iScience

CellPress

Article

Surface-Enhanced Raman Spectroscopy on Amorphous Semiconducting Rhodium Sulfide Microbowl Substrates

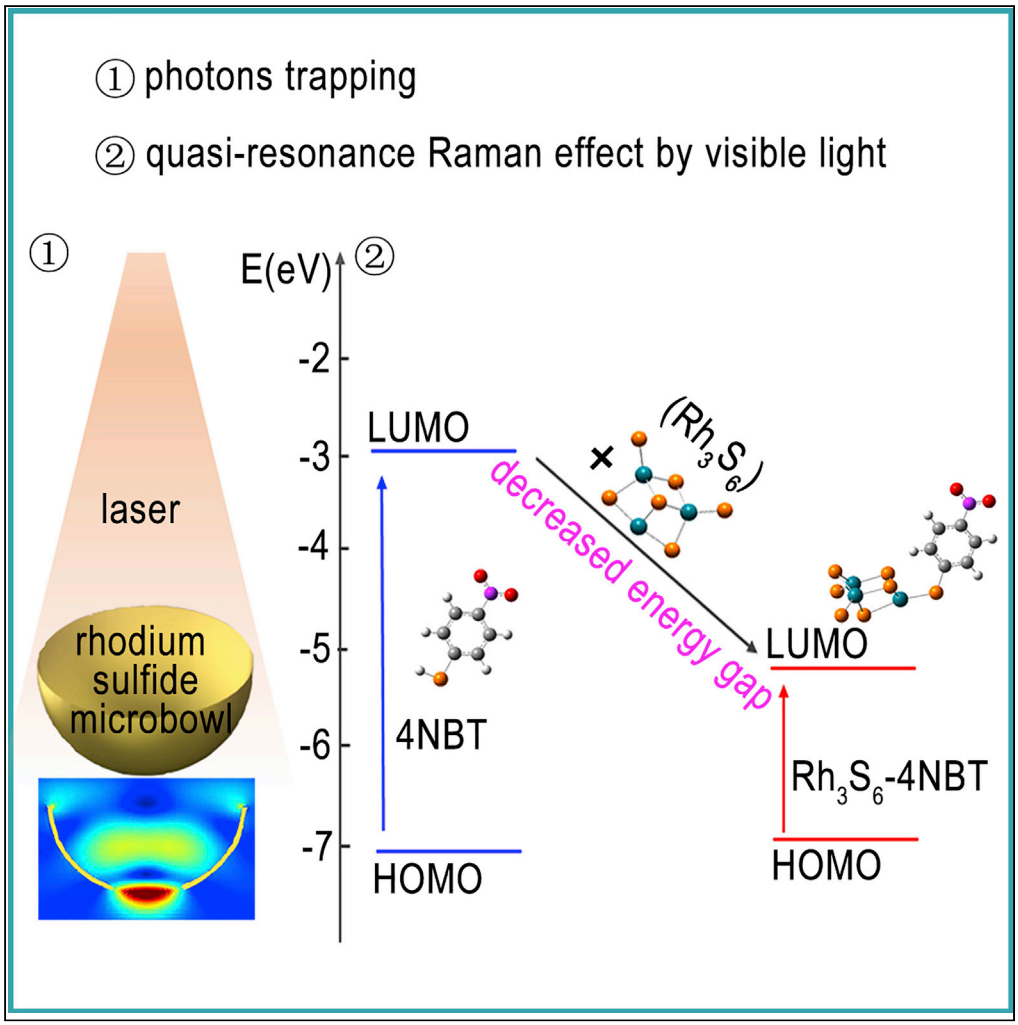

Anran Li, Jie Lin, Zhongning Huang, Xiaotian Wang, Lin Guo

wangxt@buaa.edu.cn (X.W.)
guolin@buaa.edu.cn (L.G.)

HIGHLIGHTS

Surface-enhanced Raman scattering (SERS) on amorphous semiconducting rhodium sulfide

High SERS enhancement factor and low limit of detection have been achieved

Decreased energy gap enables quasi-resonance Raman effect by visible light

Bowl-like shape enables multiple light scattering for efficient photon trapping

Li et al., iScience *10*, 1–10
December 21, 2018
https://doi.org/10.1016/j.isci.2018.11.017

iScience

CellPress

Article

Surface-Enhanced Raman Spectroscopy on Amorphous Semiconducting Rhodium Sulfide Microbowl Substrates

Anran Li,[1,2,3] Jie Lin,[1,2,3] Zhongning Huang,[1,2,3] Xiaotian Wang,[1,2,*] and Lin Guo[1,2,4,*]

SUMMARY

Exploring highly surface-enhanced Raman scattering (SERS)-active semiconductors is urgently required for practical applications. Here, with the guidance of theoretical calculations, amorphous rhodium sulfide microbowls with high enhancement factor (1×10^5) and low limit of detection (10^{-7} M) for rhodamine 6G are successfully developed. This remarkable sensitivity is attributed to quasi-resonance Raman effect and multiple light scattering. The first-principles calculations show that the energy gap of 4-nitrobenzenethiol adsorbed on Rh_3S_6 is greatly decreased by shifting its lowest unoccupied molecular orbital (LUMO) energy level close to the LUMO of Rh_3S_6, enabling quasi-resonance Raman effect by visible light. The finite-difference time-domain simulations demonstrate the efficient photon trapping ability enabled by multiple light scattering. The optimum wavelength of ~633 nm for SERS is predicted in simulations and confirmed in experiments. Our results provide both a deep insight of the photo-driven charge transfer process and an important guidance for designing SERS-active semiconductors.

INTRODUCTION

Surface-enhanced Raman scattering (SERS) spectroscopy is a powerful analytical tool in chemical and biological sensing, especially in the fields of food security and environment science, because it enables a highly sensitive, non-destructive, label-free detection with quick response and can provide molecular fingerprints of the adsorbates (Alessandri and Lombardi, 2016; Laing et al., 2017; Stiles et al., 2008). In the past, noble metal nanoparticles (NPs) were traditionally used as effective SERS substrates, where the electromagnetic enhancement mechanism plays a dominant role (Guerrini and Graham, 2012; Li and Li, 2014; Li et al., 2017; Rycenga et al., 2011). Nevertheless, the high cost, poor biocompatibility, and spectra uniformity of noble metal NPs severely limit their practical applications in SERS (Cong et al., 2015; Liu et al., 2018; Zheng et al., 2017).

Therefore, semiconductor-based SERS substrates with low cost, good spectra reproducibility, and biocompatibility have attracted increasing attention, greatly expanding the applications of SERS spectroscopy in various fields. However, the enhancement factor (EF) of semiconductor-based SERS substrates is usually in the range of 10–1,000, which is too low to meet the requirement of biological and chemical sensing. In respect of this, our research group has devoted tremendous efforts to investigate novel semiconductor nanomaterials with improved SERS activity, such as ZnO nanosheets (Liu et al., 2014), SnO_2 NPs (Jiang et al., 2012), and Cu_2O NPs (Jiang et al., 2013; Lin et al., 2017, 2018). More recently, our group found that amorphous ZnO nanocages exhibited a higher SERS activity than their crystalline counterparts, ascribing to the more efficient interfacial charge transfer (CT) assisted by the metastable electronic states of amorphous ZnO nanostructures (Wang et al., 2017). Different from conventional semiconductor-based SERS studies that mainly focus on crystalline structure, our recent study opens a new frontier for developing highly sensitive SERS spectroscopy using amorphous semiconductors (Wang et al., 2017).

Despite the rapid development, exploring novel SERS-active semiconductors with high EF and low limit of detection (LOD) is still urgently required for practical applications. Generally, it is believed that the chemical enhancement mechanism dominates the SERS of semiconductors, where the photo-driven CT mechanism plays a major role (Albrecht, 1960, 1961; Lombardi and Birke, 2009; Lombardi et al., 1986; Quagliano, 2004; Wang et al., 2011; Yang et al., 2008; Yilmaz et al., 2015). Therefore, a clear understanding of the photo-driven CT process and correlating the enhanced Raman intensities with excitation wavelength are extremely important for designing sensitive semiconductor-based SERS substrates. However, the

[1]Key Laboratory of Bio-Inspired Smart Interfacial Science and Technology, Ministry of Education, School of Chemistry, Beihang University, Beijing 100191, P. R. China

[2]Beijing Advanced Innovation Center for Biomedical Engineering, Beihang University, Beijing 100191, P. R. China

[3]These authors contributed equally

[4]Lead Contact

*Correspondence: wangxt@buaa.edu.cn (X.W.), guolin@buaa.edu.cn (L.G.)

https://doi.org/10.1016/j.isci.2018.11.017

photo-driven CT mechanism has not been fully addressed hitherto, owing to the complexity of the CT process and the experimental difficulty in identifying CT states.

Herein, theoretical calculations are first performed to give a clear and deep understanding of the SERS activity of rhodium sulfide. Then, with the guidance of calculation results, amorphous rhodium sulfide microbowls combining the advantages of both amorphous structure for efficient interfacial CT and bowl-like shape for effective photon trapping are successfully developed. The first-principles calculations indicate that the bonding of 4-nitrobenzenethiol (4NBT) on the Rh_3S_6 cluster could put the lowest unoccupied molecular orbital (LUMO) of the Rh_3S_6-4NBT complex close to the LUMO of Rh_3S_6, significantly decreasing the energy gap of the complex, enabling the quasi-resonance Raman effect by visible light. Based on the CT strength rather than the oscillator strength, an optimum wavelength of around 633 nm for SERS of amorphous rhodium sulfide is predicted, which is further demonstrated in experiments. Ascribing to the quasi-resonance Raman effect and the effective light trapping, amorphous rhodium sulfide microbowls exhibit a remarkable SERS sensitivity with a high EF of 1×10^5 and a low LOD of 10^{-7} M for rhodamine 6G (R6G). Previous studies mainly focused on the SERS of metal oxide semiconductors, whereas the SERS activity of metal sulfide semiconductors has seldom been investigated (Shan et al., 2017; Zhang et al., 2017). Our work offers a cost-effective strategy for designing novel SERS-active semiconductors guided by theoretical calculations.

RESULTS AND DISCUSSION

Theoretical Prediction of the SERS Activity

As a common metal sulfide semiconductor, rhodium sulfide nanomaterials have been widely used as catalysts with excellent chemical stability and corrosion resistance. Nevertheless, their SERS activity is never reported. In this work, we first investigate the SERS activity of amorphous rhodium sulfide using the first-principles calculations performed by the Gaussian 09 package (Frisch et al., 2010). A rhodium sulfide cluster (Rh_3S_6) is built based on the pre-demonstrated model of transition metal sulfide clusters (Cakır and Gülseren, 2012; Gemming et al., 2010; Guo et al., 2016; Mayhall et al., 2011). The rhodium oxide cluster (Rh_3O_6) is also built for comparison purpose. The cluster models have been successfully used to qualitatively describe the property of amorphous structures before (Nai et al., 2015; Wang et al., 2017) and have been widely used in the SERS simulations (Jiang et al., 2013; Zhao et al., 2006). The detailed parameters for the calculations are shown in the Supporting Information. The optimized structures of the 4NBT, the Rh_3S_6 cluster, the Rh_3S_6-4NBT complex, and the Rh_3O_6-4NBT complex are shown in Figure 1A. The Rh-S bond in the Rh_3S_6 cluster is in the range of 2.1–2.34 Å, and the Rh-O bond in the Rh_3O_6 cluster is in the range of 1.7–2.0 Å. The 4NBT molecule is bonded to the Rh_3S_6 (Rh_3O_6) via the Rh-S (Rh-O) bonding (Lin et al., 2018; Yang et al., 2008). The calculation results indicate that the S atom in 4NBT is preferred to adsorb on the Rh atom numbered 2 with a relatively smaller energy of the complex.

Figure 1B shows the static Raman scattering spectra of a single 4NBT molecule, and the 4NBT adsorbed on the Rh_3S_6 and Rh_3O_6 clusters. Obviously, the Raman intensity of the 4NBT molecule is enhanced when adsorbed on either the Rh_3S_6 or the Rh_3O_6 clusters, especially for the modes at ~1,620 cm^{-1} and ~1,108 cm^{-1}, which correspond to the C=C stretching mode and the ring-breathing mode coupled to the C-S stretch mode, respectively (Figure S1). In addition, ~8 cm^{-1} and ~16 cm^{-1} red shifts of the ~1,620 cm^{-1} and ~1,108 cm^{-1} modes are observed when 4NBT is adsorbed on the Rh_3S_6 and Rh_3O_6 clusters, which is an indication of the CT process. A comparison of the Raman intensities of 4NBT for the vibration modes at 1,108 cm^{-1} and 1,620 cm^{-1} indicates that the rhodium sulfide may be a better candidate than rhodium oxide for sensitive SERS spectroscopy (Figure 1C).

To understand the higher SERS activity of rhodium sulfide, the polarizabilities and the charge difference distributions of the Rh_3S_6-4NBT complex and the Rh_3O_6-4NBT complex are calculated (Figure 1D). The redistributions of the charge density show that the Rh-S bond serves as the CT channel and facilitates the redistribution of the electron cloud around the 4NBT molecule and the Rh_3S_6 or the Rh_3O_6 clusters. The results indicate that the charge density deformation mainly happens around the C and S atoms of the 4NBT ring, which is beneficial for the chemical enhancement (Zayak et al., 2011). The Hirshfeld population analysis (Hirshfeld, 1977) indicates that 0.112 e is transferred from the Rh_3S_6 cluster to the 4NBT, whereas the amount of charge transferred from the Rh_3O_6 cluster to 4NBT is 0.013 e. The optimized geometries of the Rh_3S_6 and Rh_3O_6 clusters indicate that Rh_3O_6 exhibits a more compact structure than Rh_3S_6, resulting from the shorter Rh-O bond. The less charge exchange between Rh_3O_6 and 4NBT may come

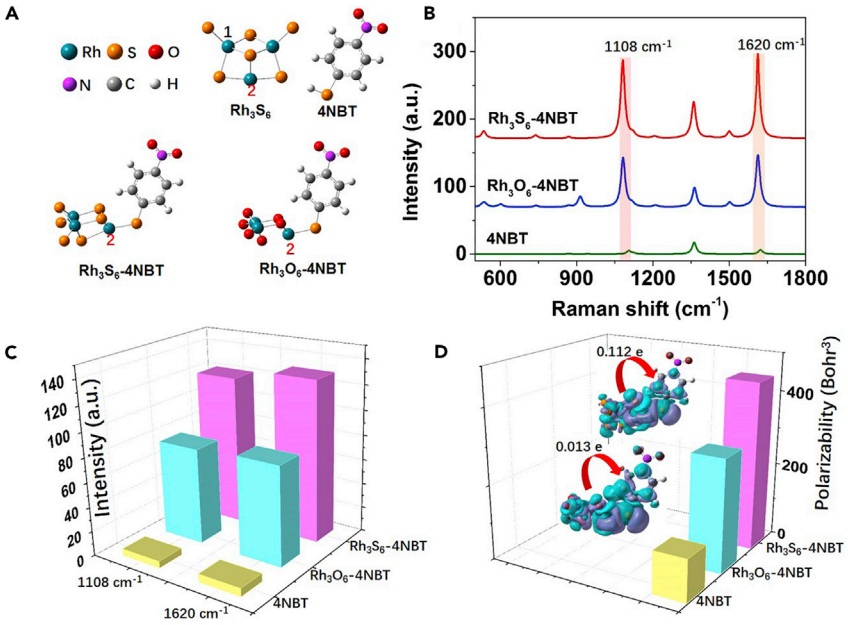

Figure 1. Theoretical Investigations on the Static Chemical Enhancement of Rh_3S_6 in SERS

(A) Basic model of the 4NBT, Rh_3S_6, Rh_3S_6-4NBT complex, and the Rh_3O_6-4NBT complex after optimization.

(B) Calculated Raman spectra of the single 4NBT molecule, the Rh_3S_6-4NBT complex, and the Rh_3O_6-4NBT complex.

(C) Comparison of the Raman intensities for the modes at 1,108 cm^{-1} and 1,620 cm^{-2}, respectively.

(D) Calculated polarizabilities of the single 4NBT, the 4NBT adsorbed on Rh_3S_6, and the Rh_3O_6, respectively. The inset in (D) shows the charge difference distributions of the Rh_3S_6-4NBT and Rh_3O_6-4NBT complexes with electrons in purple and holes in cyan (Isovalue = 0.0004).

See also Figure S1.

from the more compact structure of Rh_3O_6 and the larger electronegativity of O atoms, which could generate a greater confinement of the electrons in Rh_3O_6 and hence weakens the interaction between the electron clouds of 4NBT and Rh_3O_6. The stronger static CT from Rh_3S_6 to 4NBT could greatly increase the polarizability of the 4NBT, resulting in the highly enhanced Raman signals of 4NBT. As shown in Figure 1D, the calculated polarizabilities of the 4NBT and the 4NBT adsorbed on the Rh_3S_6 and Rh_3O_6 clusters are 112, 446, and 299 $Bohr^3$, respectively.

Besides increasing the static polarizabilities, we find that rhodium sulfide can also greatly modify the molecular orbital of the adsorbed 4NBT molecule. As shown in Figure 2A, the highest occupied molecular orbital (HOMO) and the LUMO for both the 4NBT molecule and the Rh_3S_6 cluster are distributed on the whole structure. When the 4NBT molecule is adsorbed on the Rh_3S_6 cluster, the HOMO is still delocalized on the whole complex, mainly composed by the valence sulfur p orbitals, carbon p orbitals, and rhodium d orbitals. Nevertheless, the LUMO of the complex is mainly localized on the Rh_3S_6 cluster with significant sulfur p orbital and rhodium d orbital contributions. The p and d orbitals are identified based on the shape of the orbitals shown in the calculated HUMO and LUMO images, where the p orbital exhibits a dumbbell shape and the d orbital possesses a double dumbbell shape. More importantly, we find that the LUMO energy level of the Rh_3S_6 cluster is −5.011 eV, which is between the HOMO (−2.908 eV) and LUMO (−7.012 eV) of the 4NBT. When bonding the 4NBT on the Rh_3S_6 cluster, the LUMO of the Rh_3S_6-4NBT complex is shifted close to the LUMO of Rh_3S_6. According to the calculations, the HOMO-LUMO energy gap for 4NBT is ~4.104 eV, which is too large to allow resonance Raman scattering by visible light. However, when adsorbing 4NBT onto the Rh_3S_6, the energy gap of the 4NBT is greatly decreased. The decreased energy gap enables new possible CT excitations at the low-energy level, resulting in the quasi-resonance Raman scattering effect at specific wavelength and hence efficient enhancement of the Raman signals. Generally, it is difficult to detect molecules with large energy gap due to the lack of resonance Raman effect. Our findings suggest an effective way to detect molecules with large band gaps using semiconductor substrates with proper band gaps to decrease the energy gap of the complex and enable the quasi-resonance Raman effect.

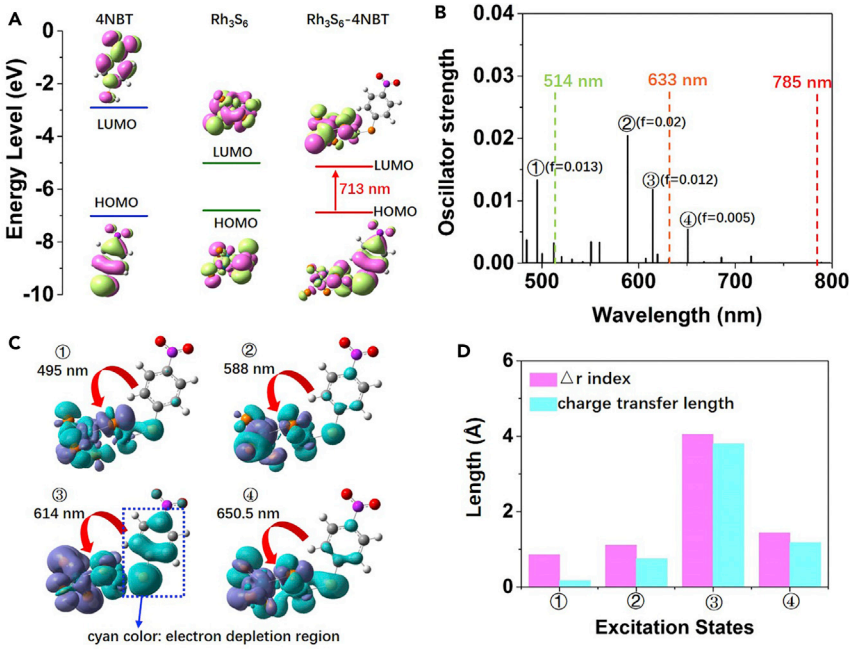

Figure 2. Theoretical Investigations on the Photo-Driven Charge Transfer Process in Rh_3S_6-4NBT

(A) Illustration of the HOMO and LUMO of 4NBT, Rh_3S_6, and Rh_3S_6-4NBT (Isovalue = 0.02).

(B) Calculated vertical transition energies and oscillator strengths of Rh_3S_6-4NBT complex; f is the oscillator strength.

(C) Charge difference densities for the singlet excitation states of Rh_3S_6-4NBT labeled with ①, ②, ③, ④ in (B); the purple and cyan stand for the electron and hole, respectively (Isovalue = 0.0004), and the red arrows indicate the charge transfer direction.

(D) The △r index and the charge transfer length of the singlet excitation states of Rh_3S_6-4NBT labeled with ①, ②, ③, ④ in (B). See also Figure S2.

Figure 2B shows the electronic excitation states of the Rh_3S_6-4NBT complex. Comparing with the electronic transition states of a 4NBT molecule (Figure S2), Figure 2B shows that the interaction between the 4NBT and the Rh_3S_6 cluster creates some new electronic transitions in the visible light region. When the incident wavelength approaches the allowed electronic transitions, the quasi-resonance Raman effect could happen through the photo-driven CT between the molecule and the semiconductor, resulting in the greatly enhanced Raman intensities. As lasers with different wavelength could excite different electronic excitation states, the SERS activity of rhodium sulfide should exhibit wavelength-dependent behavior. In previous studies, the resonance Raman intensities based on photo-driven CT mechanism were normally believed to be proportional to the square of the oscillator strength, whereas the CT strength was seldom considered (Gao et al., 2015; Lombardi and Birke, 2009; Zhao et al., 2006). To elucidate the photo-driven CT process and give a deep understanding of the wavelength-dependent SERS of rhodium sulfide, we then clearly examine both the CT strength and the oscillator strength for several representative electronic transition states. As shown in Figure 2C, the charge difference densities at the four excited states (labeled with ①, ②, ③, ④ in Figure 2B) with relatively larger oscillator strength are calculated. The results indicate that the four selected excited states could be assigned to the mixtures of the local excitation within the Rh_3S_6 cluster and the photo-driven CT excitation associated with the interband CT from the 4NBT to the Rh_3S_6 cluster. A majority of the electron transfer from the 4NBT to the Rh_3S_6 cluster can be clearly observed with the holes mainly distributed at the 4NBT part. Figure 2C visually shows that the most efficient CT from the 4NBT to the Rh_3S_6 cluster happens at mode ③ (614 nm), followed by mode ④ (650.5 nm), mode ② (588 nm), and then mode ① (495 nm). However, according to Figure 2B, the oscillator strength at mode ② is the largest, followed by mode ①, mode ③, and then mode ④. Our results indicate that the CT strength is inconsistent with the oscillator strength of the electronic transition state. Therefore, it is inappropriate to estimate the photo-induced chemical enhancement of SERS using the oscillator strength alone. To quantify the CT strength for the four selected electronic transition states of the Rh_3S_6-4NBT complex, we then calculate the CT length and the △r index, which are quantitative indicators of the electron excitation mode (Guido et al., 2013).

As shown in Figure 2D, the △r indices for modes ①, ②, ③, and ④ are 0.853 Å, 1.107 Å, 4.043 Å, and 1.436 Å, respectively. Also, the CT lengths for modes ①, ②, ③, and ④ are 0.166 Å, 0.749 Å, 3.799 Å, and 1.178 Å, respectively. These quantitative data are well matched with Figure 2C, directly demonstrating that mode ③ exhibits the strongest CT character from 4NBT to the Rh_3S_6, followed by mode ④, and then mode ② and mode ①. Based on these analysis, we predict that amorphous rhodium sulfide should generate the most enhanced Raman signals of 4NBT at the wavelength close to modes ③ (614 nm) and ④ (650.5 nm).

According to the calculated oscillator strength, one may assume that 4NBT adsorbed on the rhodium sulfide exhibits the largest SERS enhancement at the wavelength close to mode ② (588 nm), which is the general method adopted in previous studies. However, after carefully analyzing the excitation modes of each electronic transition state, we find that the CT strength is not consistent with the oscillator strength. This is because the electronic excitation states involve both the local excitation and the CT excitation, whereas only the CT between the molecules and the semiconductors contributes to the enhanced Raman signals of adsorbed molecules. Therefore, to estimate the wavelength-dependent SERS activity of semiconductors, carefully analyzing the excitation modes is necessary to identify the CT strength in each electronic transition state. Our findings give a deep understanding of the photo-driven CT process in the SERS of semiconductors and provide a novel strategy to correlate the enhanced Raman intensities with the excitation wavelength based on the quasi-resonance Raman effect, which is extremely important for selecting the optimal incident wavelength for sensitive SERS.

Synthesis, Characterization, and SERS Response

Guided by theoretical calculations, the amorphous rhodium sulfide microbowls are then designed and successfully synthesized for SERS. The detailed synthesis procedures for the amorphous rhodium sulfide microbowls are shown in the Supplemental Information. The amorphous rhodium sulfide is specifically synthesized in bowl shape to combine the advantages of both bowl-like shape and the amorphous nanostructure for highly sensitive SERS. For one thing, the amorphous structure is favorable for the more efficient interfacial CT assisted by the metastable electronic states (Wang et al., 2017). For another thing, the bowl-like shape enables effective photon trapping by multiple scattering of light (Wang et al., 2016). Figures 3A and 3B show the scanning electron microscopic images of the synthesized rhodium sulfide samples with different magnifications. The results indicate that the as-prepared rhodium sulfide samples are in bowl-like shapes with excellent size uniformity. The selected area electron diffraction pattern shown in the inset of Figure 3C directly demonstrates the amorphous structure of the rhodium sulfide sample, which is consistent with the spherical-aberration-corrected transmission electron microscopic image (Figure S3A). X-ray diffraction (XRD) also verifies the amorphous phase of the as-prepared sample, where the XRD pattern shows no distinct diffraction peaks (Figure S3B). The surface compositions of the Rh and S elements for the as-prepared samples are confirmed by X-ray photoelectron spectroscopy (XPS) (Figures S3C and S3D). The Rh $3d_{5/2}$ and Rh $3d_{3/2}$ binding energies of the amorphous rhodium sulfide microbowls are located at 309 and 313.7 eV, respectively, indicating that the rhodium existed as Rh^{4+}. The peaks of S $2p_{3/2}$ and S $2p_{1/2}$ levels at 162.7 and 163.9 eV, respectively, which are assigned to the S^{2-} ions. The XPS results are consistent with the Rh_3S_6 cluster model for which the atomic ratio of Rh and S is 1:2. All these results indicate that the amorphous rhodium sulfide microbowls have been successfully synthesized.

To demonstrate the efficient photon trapping ability of the amorphous rhodium sulfide microbowls, the electric field distributions of amorphous rhodium sulfide microbowl and amorphous rhodium sulfide film are calculated (Figure 3D). Based on the scanning electron microscopic image, the diameter and depth of the microbowl are approximately 1 and 0.5 μm. Compared with the rhodium sulfide film, intensely enhanced electric fields are observed inside the microbowl because of the multiple light scattering, directly demonstrating the effective photon-trapping ability of the microbowl structure. The intensified electric fields inside the microbowl could improve the performance of rhodium sulfide in SERS, considering that the enhancement of Raman signals is approximately proportional to $|E|/|E_0|^4$. In addition, the photon-trapping ability could be well controlled by manipulating the size of the amorphous rhodium sulfide microbowl. As shown in Figure S4, the electric field enhancement inside the microbowl gradually increases on increasing the diameter of the microbowl from 0.6 to 1 μm. With further increase in the diameter of the microbowl from 1 to 1.2 μm, an obvious decrease of the electric field enhancement within the microbowl is observed. The results indicate that in this work the microbowl with ~1 μm diameter exhibits the best photon trapping ability for SERS.

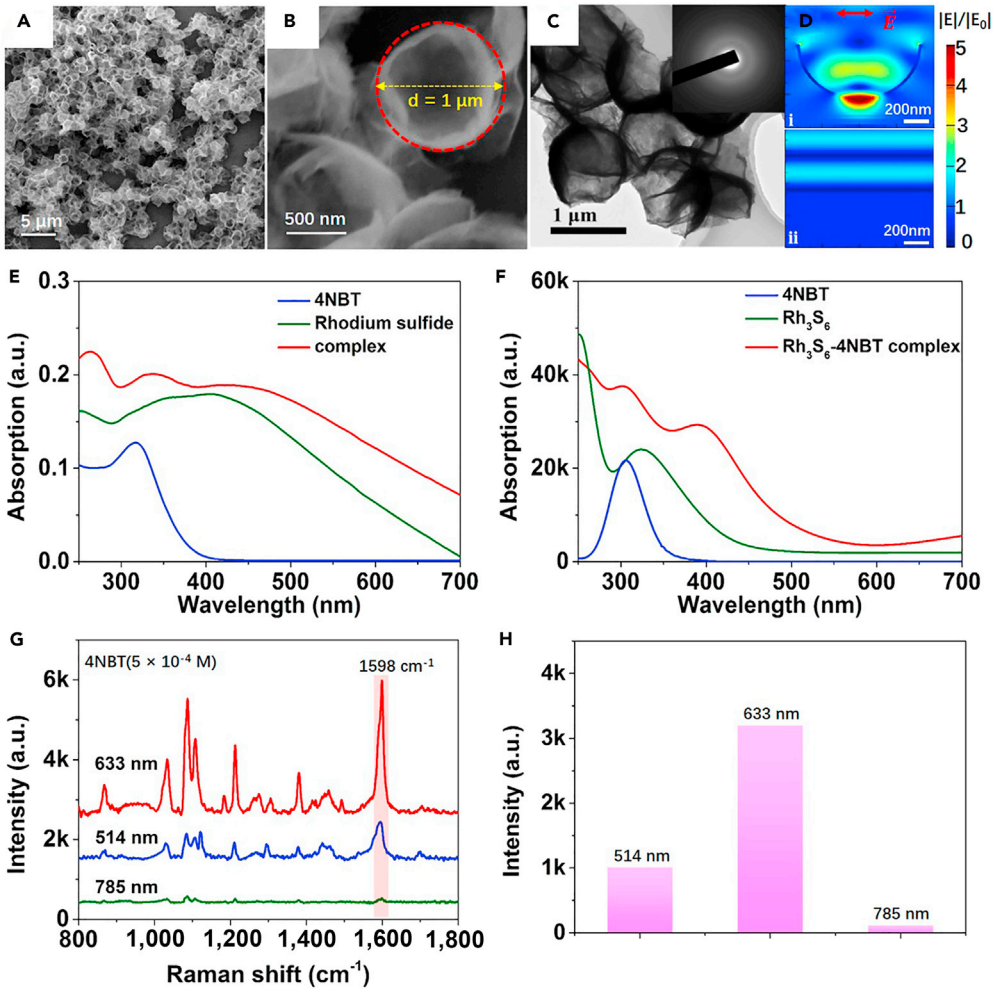

Figure 3. Characterization and SERS Response of Amorphous Rhodium Sulfide Microbowls

(A and B) Scanning electron microscopic images of amorphous rhodium sulfide microbowls with different magnifications.

(C) Transmission electron microscopic images of the amorphous rhodium sulfide microbowls with selected area electron diffraction pattern shown in inset.

(D) Calculated electric field distributions ($|E|/|E_0|$) for (i) amorphous rhodium sulfide microbowl with 1 μm diameter and 20 nm thickness and (ii) amorphous rhodium sulfide film with 20 nm thickness.

(E) Ultraviolet-visible absorption spectra of 4NBT, rhodium sulfide, and rhodium sulfide-4NBT complex in ethanol.

(F) Time-dependent density functional theory-calculated absorption spectra of a 4NBT, Rh_3S_6, and Rh_3S_6-4NBT complex in ethanol.

(G and H) SERS spectra (G) and Raman intensities of the 1,598 cm^{-1} mode (H) for 4NBT (5×10^{-4} M) adsorbed on the amorphous rhodium sulfide microbowls at different incident wavelengths.

See also Figures S3–S5.

Figures 3E and 3F show the measured and calculated absorption spectra of the 4NBT, the rhodium sulfide, and the mixture of rhodium sulfide and 4NBT. Both Figures 3E and 3F show that pure 4NBT exhibits a narrow band at the UV region, whereas the rhodium sulfide possesses a much broader band across the UV and visible light regions. In addition, a red-shifted and broadened absorption band for the mixture of 4NBT and rhodium sulfide is observed. The absorption spectra measured in experiments are well matched with the simulation results (Figure 3F), further demonstrating the rationality of the cluster model constructed here. It is also noted that the measured absorption spectrum of rhodium sulfide microbowl exhibits a broader absorption peak with a slower decay rate than the simulated one, which may be due to the influences of light scattering and bowl shape. In experiments, the measured absorption spectrum includes both the absorption and the scattering of incidence, whereas only the absorption caused by electronic transitions is counted for simulations. Figures 3E and 3F show that when 4NBT is mixed with the rhodium sulfide

microbowls, the absorption intensity at the visible light region of the complex is obviously enhanced, whereas the absorption intensity for pure 4NBT molecule in the visible light region is negligible. The red-shifted and broadened absorption peak for the mixture of 4NBT and rhodium sulfide demonstrates both the formation of rhodium sulfide-4NBT complex and the generation of new excitation states at the visible light region. The results are in good agreement with the simulation results shown in Figure 2 that the bonding of 4NBT on the Rh_3S_6 cluster could significantly decrease the energy gap of the complex and enable new possible CT excitations at the low-energy level.

We have shown in Figures 2C and 2D that 4NBT adsorbed on the rhodium sulfide is anticipated to exhibit the largest SERS intensity at the wavelength close to mode ③ (614 nm), followed by mode ④ (650.5 nm), mode ② (588 nm), and then mode ① (495 nm). With the guidance of the simulation results, the Raman intensity of 4NBT molecules adsorbed on the amorphous rhodium sulfide microbowls with 514-, 633-, and 785-nm lasers are individually measured. As shown by the green, orange, and red dashed lines in Figure 2B, the 514-nm laser is close to the excitation state ①, the 633-nm laser is close to the excitation states ③ and ④, and there is no excitation state around 785 nm. Therefore, the 633-nm laser is anticipated to generate the largest SERS enhancement because of the most efficient CT excitation, whereas enhancement of Raman signal at 785 nm should be very small mainly resulting from the static chemical enhancement. The wavelength-dependent SERS activity of amorphous rhodium sulfide microbowls is in excellent agreement with our predictions based on the simulation results. As shown in Figures 3G and 3H, the Raman intensity of 4NBT molecules is greatly enhanced for 633-nm laser, followed by 514-nm laser, and then 785-nm laser. Figure 3G shows that the vibrational modes of 4NBT at ~1,100 cm^{-1} and ~1,598 cm^{-1} are greatly enhanced when adsorbed on the surface of the amorphous rhodium sulfide microbowls, which corresponding to the ring-breathing mode coupled to the C-S stretch mode and the C=C stretching mode of the benzene ring, respectively (Shin et al., 2014). In addition, compared with the Raman spectrum of pure 4NBT (Figure S5), the position of the C=C stretching mode of 4NBT is shifted from ~1,576 cm^{-1} to ~1,598cm^{-1} when adsorbed on the amorphous rhodium sulfide microbowls, indicating the chemical enhancement mechanism associated with the CT between the rhodium sulfide substrate and the 4NBT molecule. It is also seen that the Raman intensity of ~1,360 cm^{-1} mode for the pure 4NBT molecule is much larger than that of ~1,598 cm^{-1} mode. However, when 4NBT molecules are adsorbed on amorphous rhodium sulfide microbowls, the intensity of the ~1,598 cm^{-1} mode becomes much larger than that of the 1,360 cm^{-1} mode (Figure 3G), which could be assigned to the selection rules involved in the chemical enhancement mechanism (Lombardi and Birke, 2008, 2009, 2014). Based on the equation EF = (I_{SERS}/N_{ads})/(I_{bulk}/N_{bulk}), the EF of the amorphous rhodium sulfide microbowls for 4NBT molecules at 633 nm is calculated using the intensity of the C=C stretching mode (~1,598 cm^{-1}). I_{SERS} and I_{bulk} are the SERS intensity of particular peak of the analytes and the normal Raman intensity of the analytes, and N_{ads} and N_{bulk} are the number of molecules adsorbed on the substrate and the number of molecules in normal Raman measurement. The detailed calculation procedures are shown in the Supplemental Information. According to the calculation, the EF for 4NBT molecules adsorbed on the amorphous rhodium sulfide microbowls with 633-nm laser is ~3×10^4. The results demonstrate that the photo-driven CT process plays a dominant role in the chemical enhancement of semiconductor-based SERS. For the 4NBT molecule adsorbed on Rh_3S_6 cluster without illumination, the static chemical enhancement of the C=C stretching mode is only ~20 (Figure 1). When the sample is illuminated with lasers, the SERS enhancement varies with the strength of the photo-driven CT, and the highest SERS enhancement will be obtained with the most efficient photo-driven transfer process.

Enhancement Factor and Limit of Detection

Finally, the SERS activity of the amorphous rhodium sulfide microbowls is further examined using the R6G molecules as probes. R6G molecules with a concentration of 8×10^{-5} M are used to get the EF of the R6G molecules absorbed on the amorphous rhodium sulfide microbowls. The concentration of 8×10^{-5} M is selected to avoid the supersaturated adsorption of R6G molecules on SERS substrates (Lin et al., 2017). Since the absorption band of R6G is at ~520 nm, it is better to use lasers with longer wavelength in SERS measurement of R6G to avoid the effects of absorption. Therefore, the 647-nm laser is used to examine the EF and LOD. As shown in Figure 4A, the seven characteristic bands of R6G centered at ~616 cm^{-1}, ~771 cm^{-1}, ~1,183 cm^{-2}, ~1,313 cm^{-1}, ~1,358 cm^{-1}, ~1,503 cm^{-1}, and ~1,652 cm^{-1} are clearly detected for the 8×10^{-5} M R6G adsorbed on the amorphous rhodium sulfide microbowls (Hildebrandt and Stockburger, 1984; Jensen and Schatz, 2006). Particularly, the bands centered at ~616 cm^{-1} and ~771 cm^{-1} represent an out-of-plane deformation vibration of the xanthene ring and a

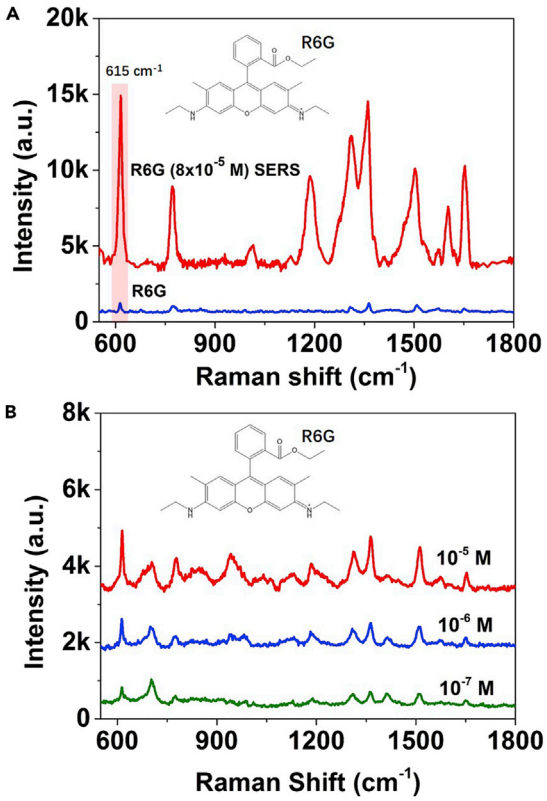

Figure 4. SERS Sensitivity of Amorphous Rhodium Sulfide Microbowls for R6G

(A) Normal Raman spectrum of R6G and SERS spectrum of R6G (8×10^{-5} M) adsorbed on the amorphous rhodium sulfide microbowls.

(B) SERS spectra of R6G molecules at different concentrations adsorbed on the amorphous rhodium sulfide microbowls, respectively. Inset shows the chemical structure of R6G. Laser wavelength: 647 nm.

See also Table S1.

C-H out-of-plane bending vibration, respectively, which may acquire the resonance Raman intensity via vibronic coupling (Hildebrandt and Stockburger, 1984). The EF of ~616 cm^{-1} mode for R6G molecules adsorbed on the amorphous rhodium sulfide microbowls is estimated to be ~1×10^5, which is higher than most of the metal oxide SERS substrates in previous studies, and is the best EF that has been achieved for metal sulfide semiconductors (Table S1). The LOD of the amorphous rhodium sulfide nanostructures for R6G molecules is also explored. As shown in Figure 4B, even when the concentration of the R6G molecules is decreased to 10^{-7} M, the characteristic bands of R6G molecules can still be obviously detected. The high EF (1×10^5) and the low LOD (10^{-7} M) of the amorphous rhodium sulfide microbowls in the SERS detection of R6G molecules further demonstrates their excellent sensitivity for SERS spectroscopy.

Conclusions

In conclusion, amorphous rhodium sulfide microbowls with excellent SERS performance are successfully designed and synthesized with the guidance of theoretical calculations. The amorphous structure is favorable for efficient interfacial CT, and the bowl-like shape is beneficial for photon trapping by multiple light scattering. The first-principles calculations of Rh_3S_6-4NBT show that the rhodium sulfide could greatly enlarge the polarizability of 4NBT. In addition, the energy gap of 4NBT adsorbed on rhodium sulfide could be greatly decreased by shifting its LUMO energy level close to the LUMO of the rhodium sulfide cluster, making new CT excitations available at the visible light region, and efficiently enhancing the Raman signals by quasi-resonance Raman effect. Based on the CT strength analysis and electric field distribution, the optimum wavelength at ~633 nm for SERS of amorphous rhodium sulfide microbowls are well predicted and confirmed in experiments. Combining the quasi-resonance Raman effect and the efficient photon trapping, the amorphous rhodium sulfide microbowls exhibit an outstanding SERS activity with a high EF of 1×10^5

and a low LOD of 10^{-7} M for R6G, which is better than that of most of the metal oxide SERS substrates in previous studies and is the best that has been achieved for metal sulfide semiconductors. Our results provide both a deep insight of the photo-driven CT mechanism in the SERS of semiconductors and a cost-effective strategy for designing SERS-active semiconductors guided by theoretical simulations and may pave the way for the development of novel semiconductor-based SERS substrates.

Limitations of the Study

At present, it is difficult to characterize the atomic structure of amorphous nanomaterials in experiments and also impossible to accurately construct the amorphous structures for simulation. Even though the cluster model built in this work is able to give an accurate qualitative description to the amorphous rhodium sulfide nanostructure, a more perfect model is needed in the future for the better description of the amorphous structures.

METHODS

All methods can be found in the accompanying Transparent Methods supplemental file.

SUPPLEMENTAL INFORMATION

Supplemental Information includes Transparent Methods, five figures, and one table and can be found with this article online at https://doi.org/10.1016/j.isci.2018.11.017.

ACKNOWLEDGMENTS

The authors gratefully acknowledge the funding from the National Natural Science Foundation of China (21875008, 51801007, 51532001) and the China Postdoctoral Science Foundation (2018M631304).

AUTHOR CONTRIBUTIONS

Conceptualization, A.L., X.W., L.G.; Investigation, A.L., J.L., and Z.H.; Writing – Original Draft, A.L.; Writing – Review & Editing, A.L., X.W., and L.G.

DECLARATION OF INTERESTS

The authors declare no competing interests.

Received: September 2, 2018
Revised: October 29, 2018
Accepted: November 8, 2018
Published: December 21, 2018

REFERENCES

Albrecht, A.C. (1960). 'Forbidden' character in allowed electronic transitions. J. Chem. Phys. *33*, 156–169.

Albrecht, A.C. (1961). On the theory of Raman intensities. J. Chem. Phys. *34*, 1476–1484.

Alessandri, I., and Lombardi, J.R. (2016). Enhanced Raman scattering with dielectrics. Chem. Rev. *116*, 14921–14981.

Cakır, D., and Gülseren, O. (2012). Ab initio study of neutral $(TiO_2)_n$ clusters and their interactions with water and transition metal atoms. J. Phys. Condens. Matter *24*, 305301.

Cong, S., Yuan, Y., Chen, Z., Hou, J., Yang, M., Su, Y., Zhang, Y., Li, L., Li, Q., Geng, F., et al. (2015). Noble metal-comparable SERS enhancement from semiconducting metal oxides by making oxygen vacancies. Nat. Commun. *6*, 7800.

Frisch, M.J., Trucks, G.W., Schlegel, H.B., Scuseria, G.E., Robb, M.A., Cheeseman, J.R., Scalmani, G., Barone, V., Mennucci, B., Petersson, A., et al. (2010). Gaussian 09, Revision C.01 (Gaussian Inc.).

Gao, Y., Chen, L., Dai, X., Song, R., Wang, B., and Wang, Z. (2015). A strong charge-transfer effect in surface-enhanced Raman scattering induced by valence electrons of actinide elements. RSC Adv. *5*, 32198–32204.

Gemming, S., Seifert, G., Götz, M., Fischer, T., and Ganteför, G. (2010). Transition metal sulfide clusters below the cluster-platelet transition: theory and experiment. Phys. Status Solidi *247*, 1069–1076.

Guerrini, L., and Graham, D. (2012). Molecularly-mediated assemblies of plasmonic nanoparticles for surface-enhanced Raman spectroscopy applications. Chem. Soc. Rev. *41*, 7085–7107.

Guido, C.A., Cortona, P., Mennucci, B., and Adamo, C. (2013). On the metric of charge transfer molecular excitations: a simple chemical descriptor. J. Chem. Theory Comput. *9*, 3118–3126.

Guo, Y., Li, J.F., Niu, X., Markovits, A., and Zhang, R.Q. (2016). Composition dependent reactivity of titanium oxide clusters. Phys. Chem. Chem. Phys. *18*, 10594–10599.

Hildebrandt, P., and Stockburger, M. (1984). Surface-enhanced resonance Raman spectroscopy of Rhodamine 6G adsorbed on colloidal silver. J. Phys. Chem. *88*, 5935–5944.

Hirshfeld, F.L. (1977). Bonded-atom fragments for describing molecular charge densities. Theor. Chim. Acta *44*, 129–138.

Jensen, L., and Schatz, G.C. (2006). Resonance Raman scattering of Rhodamine 6G as calculated using time-dependent density functional theory. J. Phys. Chem. A *110*, 5973–5977.

Jiang, L., Yin, P., You, T., Wang, H., Lang, X., Guo, L., and Yang, S. (2012). Highly reproducible

surface-enhanced Raman spectra on semiconductor SnO_2 octahedral nanoparticles. ChemPhysChem *13*, 3932–3936.

Jiang, L., You, T., Yin, P., Shang, Y., Zhang, D., Guo, L., and Yang, S. (2013). Surface-enhanced Raman scattering spectra of adsorbates on Cu_2O nanospheres: charge-transfer and electromagnetic enhancement. Nanoscale *5*, 2784–2789.

Laing, S., Jamieson, L.E., Faulds, K., and Graham, D. (2017). Surface-enhanced Raman spectroscopy for in vivo biosensing. Nat. Rev. Chem. *1*, 0060.

Li, A., and Li, S. (2014). Large-volume hot spots in gold spiky nanoparticle dimers for high-performance surface-enhanced spectroscopy. Nanoscale *6*, 12921–12928.

Li, J., Zhang, Y., Ding, S., Panneerselvam, R., and Tian, Z. (2017). Core-shell nanoparticle-enhanced Raman spectroscopy. Chem. Rev. *117*, 5002–5069.

Lin, J., Hao, W., Shang, Y., Wang, X., Qiu, D., Ma, G., Chen, C., Li, S., and Guo, L. (2018). Direct experimental observation of facet-dependent SERS of Cu_2O polyhedra. Small *14*, 1703274.

Lin, J., Shang, Y., Li, X., Yu, J., Wang, X., and Guo, L. (2017). Ultrasensitive SERS detection by defect engineering on single Cu_2O superstructure particle. Adv. Mater. *29*, 1604797.

Liu, D., Chen, X., Hu, Y., Sun, T., Song, Z., Zheng, Y., Cao, Y., Cai, Z., Cao, M., Peng, L., et al. (2018). Raman enhancement on ultra-clean graphene quantum dots produced by quasi-equilibrium plasma-enhanced chemical vapor deposition. Nat. Commun. *9*, 193.

Liu, Q., Jiang, L., and Guo, L. (2014). Precursor-directed self-assembly of porous ZnO nanosheets as high-performance surface-enhanced Raman scattering substrate. Small *10*, 48–51.

Lombardi, J.R., and Birke, R.L. (2008). A unified approach to surface-enhanced Raman spectroscopy. J. Phys. Chem. C *112*, 5605–5617.

Lombardi, J.R., and Birke, R.L. (2009). A unified view of surface-enhanced Raman scattering. Acc. Chem. Res. *42*, 734–742.

Lombardi, J.R., and Birke, R.L. (2014). Theory of surface-enhanced Raman scattering in semiconductors. J. Phys. Chem. C *118*, 11120–11130.

Lombardi, J.R., Birke, R.L., Lu, T., and Xu, J. (1986). Charge-transfer theory of surface enhanced Raman spectroscopy: Herzberg-Teller contributions. J. Chem. Phys. *84*, 4174–4180.

Mayhall, N.J., Becher, E.L., III, Chowdhury, A., and Raghavachari, K. (2011). Molybdenum oxides versus molybdenum sulfides: geometric and electronic structures of $Mo_3X_y^-$ (X = O, S and y = 6, 9) clusters. J. Phys. Chem. A *115*, 2291–2296.

Nai, J., Yin, H., You, T., Zheng, L., Zhang, J., Wang, P., Jin, Z., Tian, Y., Liu, J., Tang, Z., et al. (2015). Efficient electrocatalytic water oxidation by using amorphous Ni-Co double hydroxides nanocages. Adv. Energy Mater. *5*, 1401880.

Quagliano, L.G. (2004). Observation of molecules adsorbed on III-V semiconductor quantum dots by surface-enhanced Raman scattering. J. Am. Chem. Soc. *126*, 7393–7398.

Rycenga, M., Cobley, C.M., Zeng, J., Li, W., Moran, C.H., Zhang, Q., Qin, D., and Xia, Y. (2011). Controlling the synthesis and assembly of silver nanostructures for plasmonic applications. Chem. Rev. *111*, 3669–3712.

Shan, Y., Zheng, Z., Liu, J., Yang, Y., Li, Z., Huang, Z., and Jiang, D. (2017). Niobium pentoxide: a promising surface-enhanced Raman scattering active semiconductor substrate. NPJ Comput. Mater. *3*, 11.

Shin, K.S., Cho, Y.K., and Kim, K. (2014). Surface-enhanced Raman scattering characteristics of 4-nitrobenzenethiol adsorbed on palladium and silver thin films. Vib. Spectrosc. *70*, 120–124.

Stiles, P.L., Dieringer, J.A., Shah, N.C., and Van Duyne, R.P. (2008). Surface-enhanced Raman spectroscopy. Annu. Rev. Anal. Chem. (Palo Alto Calif). *1*, 601–626.

Wang, W., Dong, J., Ye, X., Li, Y., Ma, Y., and Qi, L. (2016). Heterostructured TiO2 nanorod@nanobowl arrays for efficient photoelectrochemical water splitting. Small *12*, 1469–1478.

Wang, X., Shi, W., Jin, Z., Huang, W., Lin, J., Ma, G., Li, S., and Guo, L. (2017). Remarkable SERS activity observed from amorphous ZnO nanocages. Angew. Chem. Int. Ed. *56*, 9851–9855.

Wang, X., Shi, W., She, G., and Mu, L. (2011). Using Si and Ge nanostructures as substrates for surface-enhanced Raman scattering based on photoinduced charge transfer mechanism. J. Am. Chem. Soc. *133*, 16518–16523.

Yang, L., Jiang, X., Ruan, W., Zhao, B., Xu, W., and Lombardi, J.R. (2008). Observation of enhanced Raman scattering for molecules adsorbed on TiO_2 nanoparticles: charge-transfer contribution. J. Phys. Chem. C *112*, 20095–20098.

Yilmaz, M., Ozdemir, M., Erdogan, H., Tamer, U., Sen, U., Facchetti, A., Usta, H., and Demirel, G. (2015). Micro-/nanostructured highly crystalline organic semiconductor films for surface-enhanced Raman spectroscopy applications. Adv. Funct. Mater. *25*, 5669–5676.

Zayak, A.T., Hu, Y.S., Choo, H., Bokor, J., Cabrini, S., Schuck, P.J., and Neaton, J.B. (2011). Chemical Raman enhancement of organic adsorbates on metal surfaces. Phys. Rev. Lett. *106*, 083003.

Zhang, Q., Li, X., Ma, Q., Zhang, Q., Bai, H., Yi, W., Liu, J., Han, J., and Xi, G. (2017). A metallic molybdenum dioxide with high stability for surface enhanced Raman spectroscopy. Nat. Commun. *8*, 14903.

Zhao, L., Jensen, L., and Schatz, G.C. (2006). Pyridine-Ag20 cluster: a model system for studying surface-enhanced Raman scattering. J. Am. Chem. Soc. *128*, 2911–2919.

Zheng, Z., Cong, S., Gong, W., Xuan, J., Li, G., Lu, W., Geng, F., and Zhao, Z. (2017). Semiconductor SERS enhancement enabled by oxygen incorporation. Nat. Commun. *8*, 1993.

ISCI, Volume *10*

Supplemental Information

Surface-Enhanced Raman Spectroscopy on Amorphous Semiconducting Rhodium Sulfide Microbowl Substrates

Anran Li, Jie Lin, Zhongning Huang, Xiaotian Wang, and Lin Guo

Supplemental Information

1. Supplemental Data Items

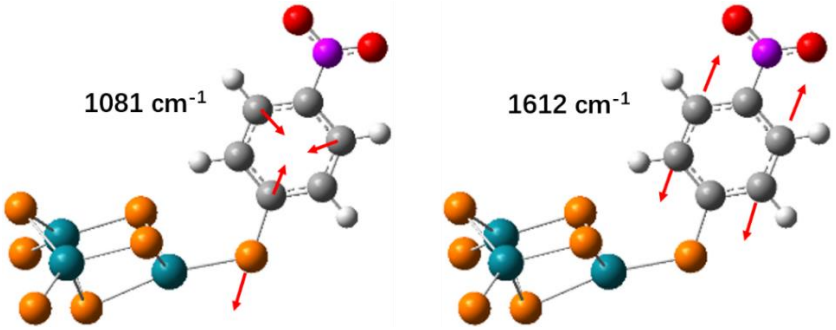

Figure S1. Calculation of the normal modes for 4NBT adsorbed on Rh_3S_6 cluster, related to Figure 1. Calculation of the ~ 1081 cm^{-1} and ~ 1612 cm^{-1} modes, corresponding to the ring-breathing mode coupled to the C-S stretch mode and the C=C stretching mode, respectively.

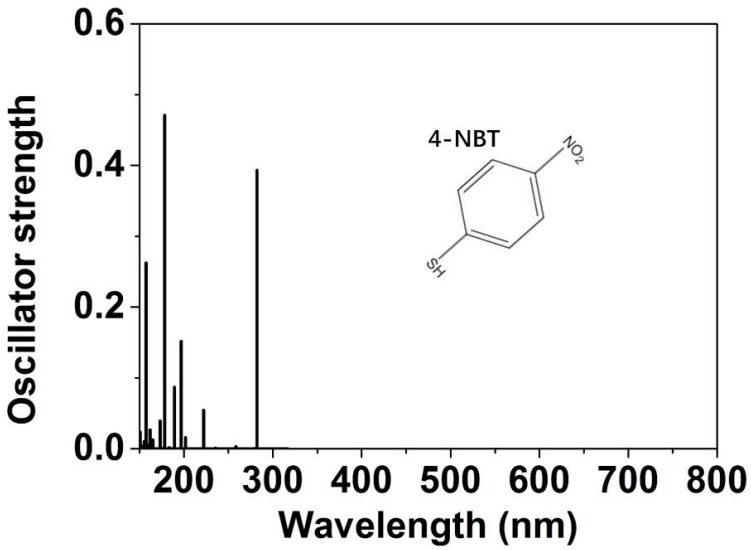

Figure S2. TDDFT calculation of a 4NBT molecule, related to Figure 2. Calculated vertical transition energies and oscillator strength of a 4NBT molecule.

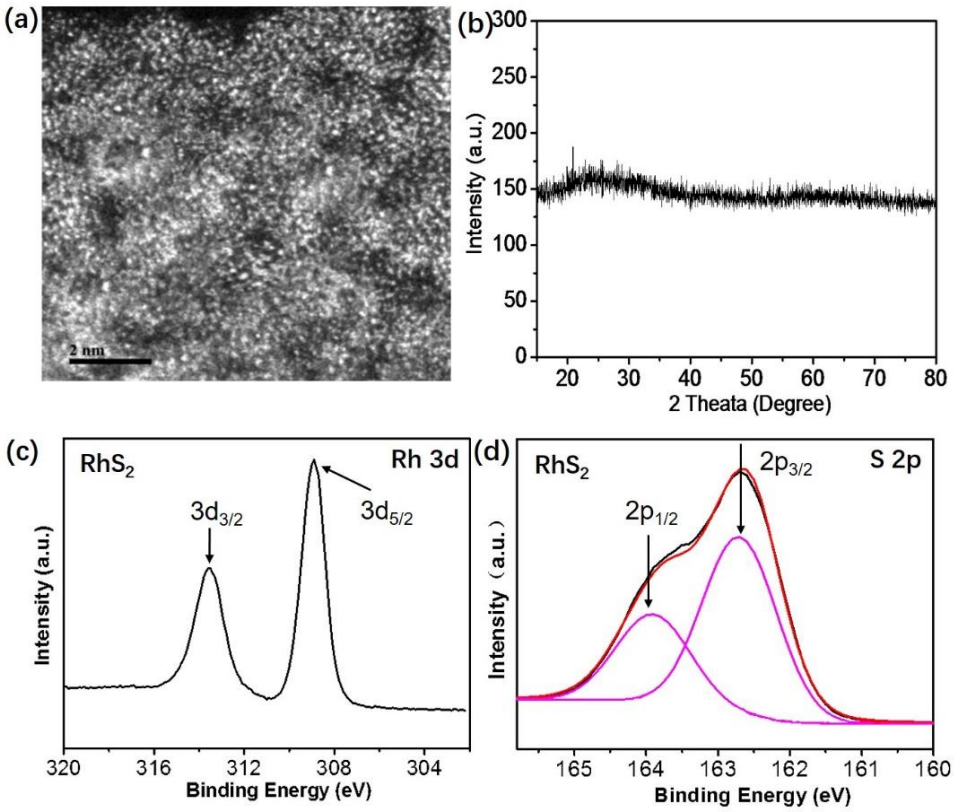

Figure S3. Characterization of the synthesized amorphous rhodium sulfide microbowls, related to Figure 3. (a) The Spherical Aberration Corrected Transmission Electron Microscope (ACTEM) image of the amorphous rhodium sulfide microbowls. (b) X-ray Diffraction (XRD) of the amorphous rhodium sulfide microbowls. (c and d) X-ray photoelectron spectroscopy (XPS) spectra of the amorphous rhodium sulfide microbowls.

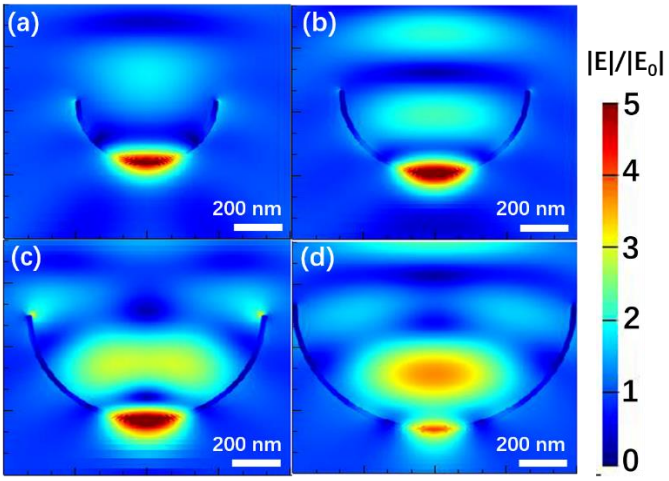

Figure S4. FDTD calculation of the amorphous rhodium sulfide microbowls, related to Figure 3. Calculated electric field distributions ($|E|/|E_0|$) for amorphous rhodium sulfide microbowls with various diameters. (a) 0.6 μm (b) 0.8 μm (c) 1 μm and (d) 1.2 μm.

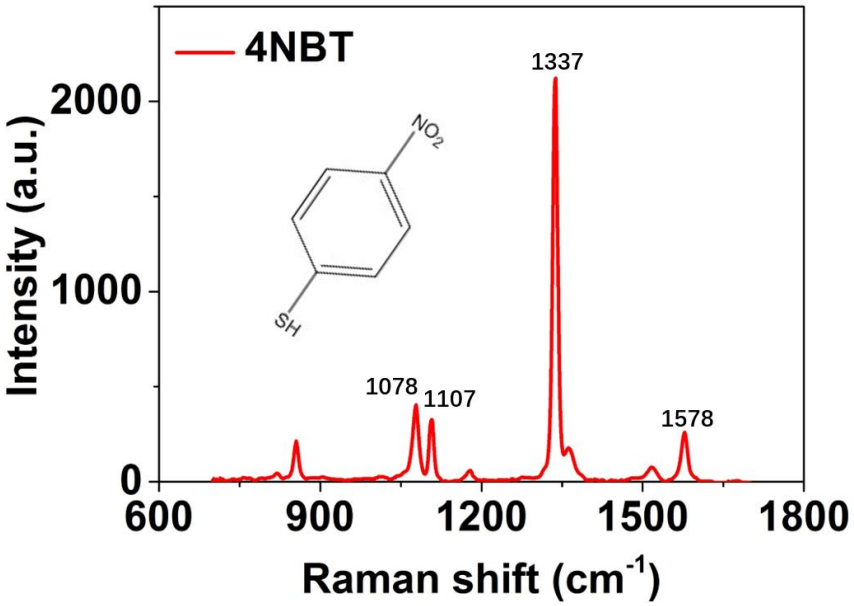

Figure S5. Normal Raman spectrum of the 4NBT at the concentration of 1 × 10^{-2} mol/L at 633 nm, related to Figure 3. The main peaks at 1578 cm^{-1}, 1337 cm^{-1}, and ~ 1100 cm^{-1} were attributed to the C=C stretching mode of the benzene ring, the symmetric stretching vibration of the nitro group (NO_2), and the ring-breathing mode coupled to the C-S stretch mode, respectively (Shin et al., 2014).

Table S1. Enhancement factor (EF) and limit of detection (LOD) of various semiconductors in previous reports (Cong et al., 2015; Jiang et al., 2013; Liu et al., 2014; Qi et al., 2014; Wang et al., 2017; Wang et al., 2011; Zheng et al., 2017). Results in this work is in bold. **Related to Figure 4.**

Material	Analyte	EF	LOD (M)	Laser (nm)	Reference
amorphous rhodium sulfide	**R6G**	**1 × 10^5**	**10^{-7}**	**647**	**this work**
amorphous ZnO	4-MBA	6.62 × 10^5	---	633	Wang et al., 2017
urchin-like $W_{18}O_{49}$	R6G	3.4 × 10^5	10^{-7}	522	Cong et al., 2015
ZnO nanosheet	4-MBA	---	10^{-6}	514.5	Liu et al., 2014
TiO_2 microarray	MB	2 × 10^4	6 × 10^{-6}	532	Qi et al., 2014
H-Si/H-Ge	R6G/N719	8-28	10^{-6}	532	Wang et al., 2011
Cu_2O nanosphere	4-MBA	10^5	10^{-3}	488	Jiang et al., 2013
MoS_2	R6G	9 × 10^3	---	532.8	Zheng et al., 2017
partially oxidized MoS_2 (optimum)	R6G	1.4 × 10^5	10^{-7}	532.8	Zheng et al., 2017
WS_2	R6G	2.5 × 10^4	---	532.8	Zheng et al., 2017

2. Transparent Methods

2.1 Computational Details

First-principles calculations: The density functional theory (DFT) and time-dependent density functional theory (TDDFT) calculations are employed to investigate the chemical enhancement mechanism of amorphous rhodium sulfide nanomaterial in surface-enhanced Raman scattering (SERS), including the geometry optimizations, ground-state properties, static Raman spectra, and vertical electronic transitions. All the calculations are implemented with the Gaussian 09 package (Frisch et al., 2010). A rhodium sulfide cluster (Rh_3S_6) and a rhodium oxide cluster (Rh_3O_6) are built based on the pre-demonstrated model of transition metal sulfide clusters (Cakır and Gülseren, 2012; Gemming et al., 2010; Guo et al., 2016; Mayhall et al., 2011). The Becke's three-parameter hybrid exchange functional and Lee,

Yang, and Parr's (B3LYP) exchange functional combined with the mixed basis sets are adopted for the structure optimization, and the calculation of the Raman spectra, the charge distribution, and the molecular orbital (Becke, 1993; Lee et al., 1988; Miehlich et al., 1989). The basis set for C, H, O, N, S atoms is 6-311+G (d,p), which includes the polarization function and the diffuse function. For Rh atom, the Lanl2dz(Hay and Wadt, 1985) basis set is used to describe its valence electrons and internal shells. The B3LYP/6-311+G(d,p) level and B3LYP/Lanl2dz level have been shown to be adequate describing the interaction of organic molecule and the transition metal sulfide cluster before. The TDDFT with the CAM-B3LYP functional is used to calculate the oscillator strength, which has been demonstrated to give a good accuracy in calculating the excited state energies (Mohammadpour and Jamshidi, 2016). In this study, all models are firstly fully optimized without imaginary frequency, guaranteeing that all the structures are in stable states. The calculated Raman spectra are broadened using a Lorentzian function with the full width at half maximum (FWHM) of 10 cm^{-1}. The calculated absorption spectra are broadened using a Gaussian function with the FWHM of 0.6 eV.

Finite-difference time-domain simulations: The electric field distributions ($|E|/|E_0|$) of amorphous rhodium sulfide microbowls and amorphous rhodium sulfide film are calculated using the 3D finite-difference time-domain (FDTD) method (Taflove and Hagness, 2005). For all simulations, a total-field scattered-field plane wave source is used to estimate the interaction between propagating plane waves and rhodium sulfide structures. Vacuum is taken as the external medium. The refractive index of amorphous rhodium sulfide is set at 4. The diameter and the wall thickness of the microbowl is 1 μm and 20 nm, respectively. The thickness of the rhodium sulfide film is 20 nm. To get accurate results, all structures are enclosed by an override mesh region with 2 nm mesh size. The incident wavelength is 633 nm. All the calculations are performed using the Lumerical Solutions (FDTD solutions 8.6, Lumerical solutions, Inc., Vancouver, Canada).

2.2 Experimental Procedures

Reagents: rhodium(III) chloride hydrate ($RhCl_3 \cdot 3H_2O$) is purchased from Alfa Aesar. Dimethyl sulfoxide (DMSO) is purchased from J&K Chemicals. The 98% concentrated sulphuric acid (H_2SO_4) is purchased from Beijing Chemical Works. The 30% hydrogen peroxide (H_2O_2) is purchased from Xilong Chemical Co., Ltd. All chemical reagents used in this experiment are analytical grade and used without further purification.

Preparation of the amorphous rhodium sulfide microbowls: The amorphous rhodium sulfide microbowls are synthesized via a hydrothermal method. In a typical synthesis, 1 mL 10 mg/mL rhodium(III) chloride hydrate is mixed with 30 mL dimethyl sulfoxide in a 100 mL flask at room temperature. The mixture is transferred into a water-bath which is kept at 20 ℃ for 10 min. Then, 3.4 mL 30% H_2O_2 is added into the flask. After being stirred for 30 min, 4.5 mL 2 mol/L H_2SO_4 is poured into the above solution, and the mixture is continuously maintained at 20 ℃ for 60 min afterwards. Subsequently, the flask is heated to 140 ℃ with oil-bath for 100 min under the magnetic stirring. After that, the mixture is centrifuged at 8000 rpm for 5 min and washed with ethanol for three times. Finally, the bowl-like rhodium sulfide nanomaterials in yellow color are obtained.

Characterization: The morphology and size of three-dimensional rhodium sulfide microbowls are characterized by scanning electron microscopy (SEM, 10kV, Quanta 250 FEG, FEI) and transmission electron microscopy (TEM, 200kV, JEM2100, JEOL). XRD patterns was performed by LabX XRD-6000.

SERS measurements: 4-nitro benzene thiol (4NBT) and rhodamine 6G (R6G) molecules are chosen as Raman target molecules. 50 μL amorphous rhodium sulfide ethanol suspension is mixed with the 4NBT and R6G molecules dispersed in ethanol solution with different concentrations, respectively. The mixtures are placed for 5 hours and then 5 μL of the mixed solution is dropped onto a clean Si substrate. The Si substrate is thoroughly rinsed for several times using the absolute ethanol to remove the free unabsorbed probe molecules. The Si samples are then subjected to Raman characterization. For all SERS measurements, 100 × objective, 0.8 mW power, and 10 s acquisition time are used to acquire the SERS spectra with 514 nm, 633 nm, 647 nm, and 785 nm excitation wavelengths. In addition, for each measurement, twenty SERS spectra from different randomly chosen positions are collected and then averaged for the final analysis.

2.3 Calculation of the SERS enhancement factor

The enhancement factor (EF) of the amorphous rhodium sulfide microbowls in SERS is calculated based on the equation $EF = (I_{SERS}/N_{ads})/(I_{bulk}/N_{bulk})$, where I_{SERS} and I_{bulk} are the SERS intensity of particular peak of the probe molecule and the normal Raman intensity of the probe molecule; N_{ads} and N_{bulk} are the number of the

molecules adsorbed on the SERS substrate and the number of molecules in normal Raman measurement.

For 4NBT molecules, the intensity of the C=C stretching mode (~ 1576 cm^{-1}) is used to calculate the EF. In the experiment, 5 μL 4NBT ethanol solution with the concentration of 1×10^{-2} mol/L is dried onto the Si wafer (0.3×0.3 cm^2). The diameter of the laser spot is $d = 1.22\ \lambda/N_A$, where λ is incident wavelength of 633 nm, N_A is the numerical aperture of the objective lens with the value of 0.5. Therefore, the laser spot size ($\pi\ (d/2)^2$) is ~ 1.87 μm^2. Then, N_{bulk} is estimated to be:

$N_{bulk} = 5\ \mu L \times 1 \times 10^{-2}$ mol/L $\times\ 6.02 \times 10^{23}$ $mol^{-1} \times 1.87\ \mu m^2 / 0.09\ cm^2 = 6.25 \times 10^9$.

For determining the N_{ads}, we assume that the 4NBT molecules are adsorbed on the rhodium sulfide as a monolayer with the molecular footprint of ~ 0.7 nm^2 (Wang and Rothberg, 2005). Therefore, N_{ads} is estimated to be 2.24×10^6 considering the laser spot size and the microbowl size (approximately one microbowl within the laser spot). In addition, according to Figure 3(g) and Figure S5, I_{SERS} = 3374, and I_{bulk} = 277. Therefore, the EF for 4NBT molecules adsorbed on the amorphous rhodium sulfide microbowls is calculated to be $\sim 3 \times 10^4$.

For R6G molecules, the intensity of the band centered at ~ 616 cm^{-1} is used to calculate the EF of R6G adsorbed on the amorphous rhodium sulfide microbowls. 5 μL R6G ethanol solution with the concentration of 1×10^{-2} mol/L is dried onto the Si wafer (0.3×0.3 cm^2) for normal Raman measurement. The diameter of the laser spot is $d = 1.22\ \lambda/N_A$, where λ is incident wavelength of 647 nm, N_A is the numerical aperture of the objective lens with the value of 0.5. Therefore, the laser spot size ($\pi\ (d/2)^2$) is ~ 1.96 μm^2. Then, N_{bulk} is estimated to be:

$N_{bulk} = 5\ \mu L \times 1.0 \times 10^{-2}$ mol/L $\times\ 6.02 \times 10^{23}$ $mol^{-1} \times 1.96\ \mu m^2 / 0.09\ cm^2 = 6.56 \times 10^9$.

According to Figure 4, I_{SERS} and I_{bulk} are determined to be 11730 and 613, respectively. In addition, N_{ads} is estimated to be 1.25×10^6 by assuming the R6G molecules are adsorbed on the rhodium sulfide as a monolayer with the molecular footprint of 1.2 nm^2 (the density of ~ 0.138 nM/cm^2) (Anderson and Bard, 1995). Therefore, the EF of R6G molecules adsorbed on the amorphous rhodium sulfide microbowls is estimated to be $\sim 1 \times 10^5$.

3. Supplemental References

Anderson, C., and Bard, A.J. (1995). An Improved Photocatalyst of TiO2/SiO2 Prepared by a Sol-Gel Synthesis. J. Phys. Chem. *99*, 9882-9885.

Becke, A.D. (1993). Density−functional thermochemistry. III. The role of exact exchange. J. Chem. Phys. *98*, 5648-5652.

Hay, P.J., and Wadt, W.R. (1985). Ab initio effective core potentials for molecular calculations. Potentials for K to Au including the outermost core orbitals. J. Chem. Phys. *82*, 299-310.

Lee, C., Yang, W., and Parr, R.G. (1988). Development of the Colle-Salvetti correlation-energy formula into a functional of the electron density. Phys. Rev. B: Condens. Matter *37*, 785-789.

Miehlich, B., Savin, A., Stoll, H., and Preuss, H. (1989). Results obtained with the correlation energy density functionals of becke and Lee, Yang and Parr. Chem. Phys. Lett. *157*, 200-206.

Mohammadpour, M., and Jamshidi, Z. (2016). Comparative assessment of density functional methods for evaluating essential parameters to simulate SERS spectra within the excited state energy gradient approximation. J. Chem. Phys. *144*, 194302.

Qi, D., Lu, L., Wang, L., and Zhang, J. (2014). Improved SERS sensitivity on plasmon-free TiO_2 photonic microarray by enhancing light-matter coupling. J. Am. Chem. Soc. *136*, 9886-9889.

Taflove, A., and Hagness, S.C. (2005). Computational electrodynamics : the finite-difference time-domain method (Boston : Artech House, c2005. 3rd ed.).

Wang, Z., and Rothberg, L.J. (2005). Origins of Blinking in Single-Molecule Raman Spectroscopy. J. Phys. Chem. B *109*, 3387-3391.